J. Non-Newtonian Fluid Mech. 160 (2009) 31–39

Contents lists available at ScienceDirect

Journal of Non-Newtonian Fluid Mechanics

journal homepage: www.elsevier.com/locate/jnnfm

Purely elastic flow asymmetries in flow-focusing devices

M.S.N. Oliveira[a,*], F.T. Pinho[b], R.J. Poole[c], P.J. Oliveira[d], M.A. Alves[a]

[a] Departamento de Engenharia Química, CEFT, Faculdade de Engenharia da Universidade do Porto, Rua Dr. Roberto Frias, 4200-465 Porto, Portugal
[b] Departamento de Engenharia Mecânica e Gestão Industrial, CEFT, Faculdade de Engenharia da Universidade do Porto, Rua Dr. Roberto Frias, 4200-465 Porto, Portugal
[c] Department of Engineering, University of Liverpool, Brownlow Street, Liverpool, L69 3GH, United Kingdom
[d] Departamento de Engenharia Electromecânica, Unidade Materiais Têxteis e Papeleiros, Universidade da Beira Interior, 6201-001 Covilhã, Portugal

ARTICLE INFO

Article history:
Received 21 July 2008
Received in revised form 18 February 2009
Accepted 24 February 2009

Keywords:
Elastic asymmetry
Converging flow
Creeping flow
Viscoelastic fluid
PTT model
UCM model

ABSTRACT

The flow of a viscoelastic fluid through a microfluidic flow-focusing device is investigated numerically with a finite-volume code using the upper-convected Maxwell (UCM) and Phan-Thien–Tanner (PTT) models. The conceived device is shaped much like a conventional planar "cross-slot" except for comprising three inlets and one exit arm. Strong viscoelastic effects are observed as a consequence of the high deformation rates. In fact, purely elastic instabilities that are entirely absent in the corresponding Newtonian fluid flow are seen to occur as the Deborah number (*De*) is increased above a critical threshold. From two-dimensional numerical simulations we are able to distinguish two types of instability, one in which the flow becomes asymmetric but remains steady, and a subsequent instability at higher *De* in which the flow becomes unsteady, oscillating in time. For the UCM model, the effects of the geometric parameters of the device (e.g. the relative width of the entrance branches, *WR*) and of the ratio of inlet average velocities (*VR*) on the onset of asymmetry are systematically examined. We observe that for high velocity ratios, the critical Deborah number is independent of *VR* (e.g. $De_c \approx 0.33$ for $WR = 1$), but depends non-monotonically on the relative width of the entrance branches. Using the PTT model we are able to demonstrate that the extensional viscosity and the corresponding very large stresses are decisive for the onset of the steady-flow asymmetry.

1. Introduction

While Newtonian fluid flows may exhibit inertial instabilities as the Reynolds number (*Re*) increases, viscoelastic fluid flows may develop elastic instabilities as the Deborah number (*De*) increases for arbitrarily small Reynolds numbers. The latter are the subject of extensive reviews (e.g. [1,2]). Shaqfeh [2] focused on purely elastic instabilities in viscometric flows in rheometry devices, which include Taylor–Couette [3,4], parallel plate flow [5–7] and cone-and-plate flows [7,8]. These instabilities received extensive interest since they can be found in a wide variety of applications including polymer processing, lubrication and coating, and can make the nominally "viscometric" flow unsuitable for rheological measurements. The underlying mechanism that leads to such instabilities is associated with the large normal-stress differences, which depend non-linearly on flow velocity and streamline curvature. In particular, it has been shown that the tensile stress along the streamlines and the local curvature of the flow play a decisive role on the onset of purely elastic instabilities [9,10]. McKinley et al. [10] define a dimensionless criterion that must be exceeded for purely elastic instability to be observed.

The advent of microfluidics has promoted a renewed interest in purely elastic flow instabilities, which occur in the absence of inertial forces when elastic forces are very strong. The small length scales characteristic of microfluidics enable the generation of flows with high deformation rates while keeping the Reynolds number small. Conditions in microfluidic devices result in the ability to promote strong viscoelastic effects, which are not masked by fluid inertia, in dilute solutions that would otherwise exhibit Newtonian-like behavior at the equivalent macroscale. Particular attention has been given to internal stagnation point flows, such as cross-slot flows [11,12]. Pathak and Hudson [11] used flow-induced birefringence and micro-particle image velocimetry to examine the flow of wormlike micellar fluids in a microfluidic cross-slot and observed a steady-flow asymmetry at high Weissenberg numbers. Arratia et al. [12] used particle tracking velocimetry and tracer experiments to study the flow of dilute polymer solutions through a cross-slot device and observed two types of flow instabilities that occur as the Deborah number is increased. The first instability consists of a transition to steady asymmetric flow, in which the flow remains steady but spatial symmetry is broken; the second instability, in which the flow becomes time-dependent, follows at higher Deb-

* Corresponding author. Tel.: +351 22 508 1998; fax: +351 22 508 1449.
E-mail addresses: monica.oliveira@fe.up.pt (M.S.N. Oliveira), fpinho@fe.up.pt (F.T. Pinho), robpoole@liverpool.ac.uk (R.J. Poole), pjpo@ubi.pt (P.J. Oliveira), mmalves@fe.up.pt (M.A. Alves).

0377-0257/$ – see front matter © 2009 Elsevier B.V. All rights reserved.
doi:10.1016/j.jnnfm.2009.02.010

orah numbers. A similar behavior was predicted numerically by Poole et al. [13] in an analogous geometry. They used a finite-volume method to simulate the flow of a viscoelastic fluid described by the upper-convected Maxwell model, and demonstrated that the steady asymmetry can be predicted and is purely elastic in nature. In fact, they reported that inertia has a stabilizing effect, delaying the onset of asymmetric flow and reducing the magnitude of the asymmetry. Xi and Graham [14] have also performed numerical calculations to simulate viscoelastic fluid flow through a 2D cross-slot geometry at low Reynolds numbers. In their finite-element simulations, which use a FENE-P constitutive equation, the solvent viscosity ratio is high and they only predict the existence of a time-dependent instability at high Deborah numbers. Furthermore, a recent study by Rocha et al. [15], who extended the work of Poole et al. [13] by considering models other than the UCM and exploring a wider range of model parameters (such as the solvent viscosity ratio and extensibility parameter), clearly show that as the solvent viscosity ratio is increased, the critical Deborah number becomes higher and eventually the unsteady instability is reached before the pitchfork bifurcation, the outcome observed in the study of Xi and Graham [14]. It will be shown here that an identical situation arises for the flow-focusing device.

A sound physical explanation for the mechanism generating the instability reported in the experiments of Arratia et al. [12] and the simulations of Poole et al. [13] has not been fully established yet, although Poole et al. [13] presented some evidence for compressive stresses in the two incoming streams distorting the velocity field in such a way that, coupled with streamline curvature, a destabilization similar to that occurring in curvilinear Couette flow would arise. It is not the purpose of the present study to provide a definite answer regarding the generating mechanism question, rather our main motivation for using a simple flow-focusing geometry was to explore the possibility of attaining a region of constant strain-rate by making use of opposing lateral fluid streams that shape a third inlet stream flowing perpendicularly to the lateral entrances. A similar geometry has been used by Luo [16] to explore electrokinetic instability effects to promote mixing. The extensional flow in such a device is studied in detail by Oliveira et al. [17]. While examining the effect of operating and geometric parameters on the flow, we observed the onset of purely elastic instabilities similar to those mentioned previously. A rigorous characterization of the transition from steady symmetric flow to steady asymmetric flow is the main focus of this work and the numerical results are examined in Section 4. In the previous sections we layout the characteristics of the flow-focusing geometry (Section 2) and present an overview of the numerical method and computational meshes used (Section 3). We conclude the paper with a brief summary of our findings.

2. Flow geometry and dimensionless numbers

The flow-focusing device under consideration is shaped much like a conventional "cross-slot" except that it contains three inlets and one exit channel. The geometric configuration used is illustrated in Fig. 1, where the main variables are identified. The geometry is two-dimensional and symmetric about the plane $x = 0$, with the origin of the coordinate system set at the center of the geometry.

Side streams are introduced into the central mainstream through two lateral channels of equal dimensions. The width of the lateral channels (D_2) was varied from $0.3D_1$ to $2D_1$, while the width of the outlet channel (D_3) was kept equal to D_1, the width of the central inlet channel. To account for the effects of geometric parameters, we define the relative width of the entrance branches as $WR = D_2/D_1$. For all configurations tested, the length of the inlet and outlet channels was set to 30 times the central inlet channel width ($30D_1$). Increasing the channel lengths to $60D_1$ was found to have a negligible effect on the flow patterns and critical Deborah numbers.

The average velocity ratio ($VR = U_2/U_1$), defined as the ratio of the inlet average velocities in the side streams (U_2) to the average velocity in the central inlet stream (U_1), was varied between 1 and 500.

To characterize the degree of elasticity we make use of the Deborah number, which represents the ratio between the relaxation time of the fluid (λ) and a characteristic time scale of the flow (t_{flow}), here defined as:

$$De = \lambda/t_{flow} = \lambda U_2/D_1 \tag{1}$$

For a given geometry, the Deborah number was varied between 0 (corresponding to Newtonian fluid flow) and the value corresponding to the onset of time-dependent flow. For reasons of rheological simplicity, most of the results presented here are for the upper-convected Maxwell model (UCM). We also present a limited number of simulation results using the linear form of the Phan-Thien–Tanner model (PTT), for which the extra-stress tensor is given by [18]:

$$\left[1 + \frac{\lambda\varepsilon}{\eta_p}\mathrm{tr}(\boldsymbol{\tau})\right]\boldsymbol{\tau} + \lambda\overset{\nabla}{\boldsymbol{\tau}} = 2\eta_p\mathbf{D} \tag{2}$$

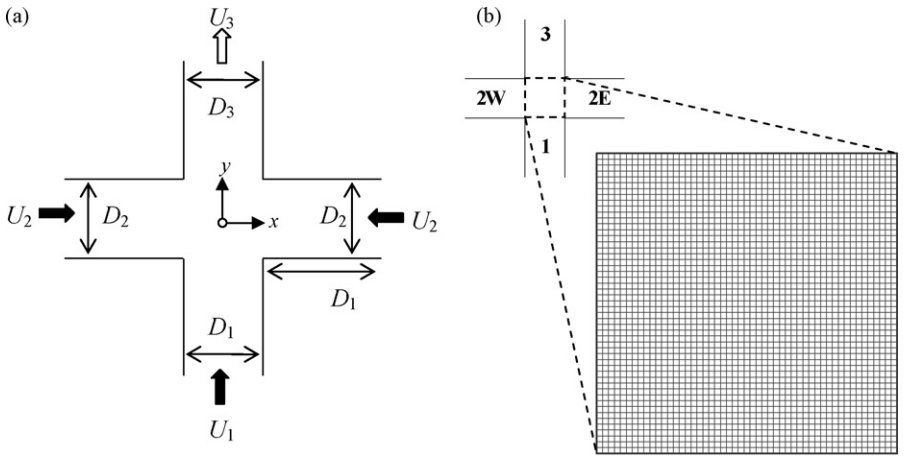

Fig. 1. (a) Schematic of the flow-focusing geometry, where U_i are mean velocities in channels of width D_i and lengths of $30D_1$; (b) details of the central region of the standard computational mesh used to map the geometry with $WR = 1$ ($\Delta x_{min} = \Delta y_{min} = 0.02D_1$).

where $\boldsymbol{\tau}$ is the elastic contribution to the extra-stress tensor, the symbol $\triangledown$ denotes the upper-convected derivative, tr($\boldsymbol{\tau}$) represents the trace of $\boldsymbol{\tau}$, η_p is the zero-shear polymer viscosity, ε is the extensibility parameter and $\mathbf{D}$ is the strain-rate tensor. The PTT model has a shear-thinning behavior, and the extensibility parameter influences significantly the extensional viscosity (increasing ε leads to a decrease of the extensional viscosity). The UCM model is a particular case that is recovered when $\varepsilon = 0$ and there is no contribution of a solvent viscosity. It exhibits constant shear viscosity as well as constant first normal-stress difference coefficient and relaxation time.

3. Numerical method and computational meshes

We consider that the flow is isothermal, incompressible and that it occurs in the absence of inertia, i.e. under creeping-flow conditions ($Re \to 0$). Even though in real flows the Reynolds number is finite and our method is capable of modeling inertial flows, Re is usually very small ($Re \ll 1$) in microfluidic flows which have characteristic length scales on the order of tens to hundreds of microns. Thus, by considering Stokes flow in the numerical simulations, we eliminate the effects of inertia and are able to isolate the effects of viscoelasticity on the flow patterns and on the potential onset of flow asymmetries. As Poole et al. [13] have shown in a related study, including a small, but finite, amount of inertia ($Re = 0.01$) has essentially no effect on the observed phenomena.

In order to model the flow in our flow-focusing device, a fully implicit finite-volume method (FVM) is used to solve the appropriate equations of conservation of mass and momentum:

$$\boldsymbol{\nabla} \cdot \mathbf{u} = 0 \tag{3}$$

$$-\boldsymbol{\nabla} p + \boldsymbol{\nabla} \cdot \boldsymbol{\tau} + \eta_s \nabla^2 \mathbf{u} = 0 \tag{4}$$

together with the constitutive equation described by Eq. (2) for the elastic contribution to the extra-stress tensor. By setting $\varepsilon = 0$ and neglecting the contribution from the solvent viscosity ($\eta_s = 0$) the UCM model is recovered. In turn, this further simplifies to a Newtonian fluid by setting $\lambda = 0$. In the above equations, $\mathbf{u}$ represents the velocity vector, p is the pressure, and $\boldsymbol{\tau}$ is an explicit function of the conformation tensor ($\boldsymbol{\tau} = (\eta_p/\lambda)(\mathbf{A} - \mathbf{I})$), i.e. instead of solving Eq. (2) we solve an equivalent form of the constitutive equation containing an evolution equation of the conformation tensor, namely:

$$\overset{\triangledown}{\lambda \mathbf{A}} = -Y(\mathrm{tr}|\mathbf{A}|)(\mathbf{A} - \mathbf{I}) \tag{5}$$

where the conformation function is $Y(\mathrm{tr}|\mathbf{A}|) = 1 + \varepsilon(\mathrm{tr}|\mathbf{A}| - 3)$. The evolution equation of the conformation tensor is solved with the log-conformation approach, which makes it possible to achieve results at higher Deborah numbers as compared to the standard formulation based on the differential equation for the extra-stress tensor [19]. As such, we have adapted our standard fully implicit FVM [20,21] to implement the log-conformation formulation of the viscoelastic constitutive equation proposed by Fattal and Kupferman [22]. This methodology in the framework of FVM is thoroughly discussed in Afonso et al. [23] and a general overview can be found in Oliveira et al. [17].

We have imposed steady-state, fully developed velocity and stress profiles at the inlet boundaries for the Newtonian and UCM runs. For the PTT runs, the analytical profiles imposed at inlet were the same as for the UCM at the same Deborah number, but it was confirmed that the flow evolves quickly (in a distance smaller than one channel width) to the actual fully developed solution for the PTT model (cf. [24] for the analytical solutions for the PTT model with a Newtonian solvent). At the outlet, we imposed Neumann boundary conditions for velocity, stresses and pressure gradient.

Table 1
Total number of cells (NC) of the standard computational meshes.

WR	0.3	0.4	0.5	0.8	1	1.25	2
NC	13,965	15,471	16,475	20,491	23,001	26,013	35,551

The length of the outlet channel was long enough for the velocity field to regain the fully developed conditions. Additionally, the no-slip condition at the walls was included. Details of implementation of boundary conditions can be found in Oliveira et al. [21].

The meshes used to map the various domains are block-structured, orthogonal and divide the central region of the geometry uniformly into cells of size $\Delta x = \Delta y \approx 0.02 D_1$, as shown in Fig. 1b. Mesh spacing is non-uniform along the cross-slot arms, tending to concentrate towards the central region. With the purpose of capturing flow asymmetries that may arise as a consequence of viscoelasticity, we map the full spatial domain except for a limited number of simulations in which symmetry was imposed along the line $x = 0$. The total number of cells (NC) varies according to the specific geometric configuration under consideration, as shown in Table 1.

Mesh refinement tests were carried out using a more refined mesh, in which the number of cells in each direction was doubled and the progression factors were square-rooted in order to consistently halve the size of each cell. Refining the mesh results in small differences in the velocity and stress profiles near the sharp corners at ($x = \pm D_1/2$, $y = -D_2/2$) and causes a slight decrease in the critical De for the transition to time-dependent flow ($\lesssim$5%). Nevertheless, mesh refinement has a negligible effect on the predicted flow patterns and on the onset of flow asymmetry. Overall, the qualitative trends obtained with the two meshes are identical and as a consequence, most calculations were performed with the base meshes of Table 1 and only those results are shown and discussed in this paper, unless otherwise stated.

4. Results and discussion

The geometry shown in Fig. 1 makes use of opposing lateral fluid streams that shape a third inlet stream which is flowing perpendicularly to the lateral entrances producing a converging flow region [17]. In order to frame the discussion and as an illustration of representative flow patterns, Fig. 2 shows the effect of Deborah number on the flow patterns for $WR = 1$ and $VR = 20$, highlighting the development of a purely elastic steady-flow asymmetry.

For low Deborah numbers, the flow is Newtonian-like remaining steady and symmetric about $x = 0$. Up to critical conditions ($De \lesssim 0.33$), the curvature of the separation streamlines near the lateral entrances is progressively enhanced as De increases. Under these conditions, the flow in the converging region displays a markedly extensional behavior as discussed in detail by Oliveira et al. [17]. Along the centerline, the fluid accelerates as it approaches the lateral entrances and a region of nearly linear velocity increase is observed in the converging section as shown in Fig. 3a for $WR = 1$, $VR = 20$ and $De = 0.1$. The dashed line in Fig. 3a highlights the region of the velocity profile with a nearly linear increase. The flow in the outlet channel quickly re-develops and a constant higher velocity is attained ($=1.5\,U_3$, corresponding to u_y/U_1 of 61.5). The corresponding streamline patterns and contour plot of the flow-type parameter are shown in Fig. 3b. The flow-type parameter ξ is used to classify the flow locally using Astarita's criterion [25] and the normalization proposed by Thompson and co-workers [26,27], $\xi \equiv (1 - R)/(1 + R)$; with R defined as $R \equiv (\mathrm{tr}(\tilde{\mathbf{W}}^2)/\mathrm{tr}(\mathbf{D}^2))$ where $\mathbf{D}$ is the strain-rate tensor and $\tilde{\mathbf{W}}$ is the relative rate of rotation tensor. As such, $\xi = +1$ corresponds to pure extensional flow, $\xi = 0$ corresponds to pure shear flow and $\xi = -1$ corresponds to pure rotational flow. Further details on the calculation of ξ can be found in Oliveira

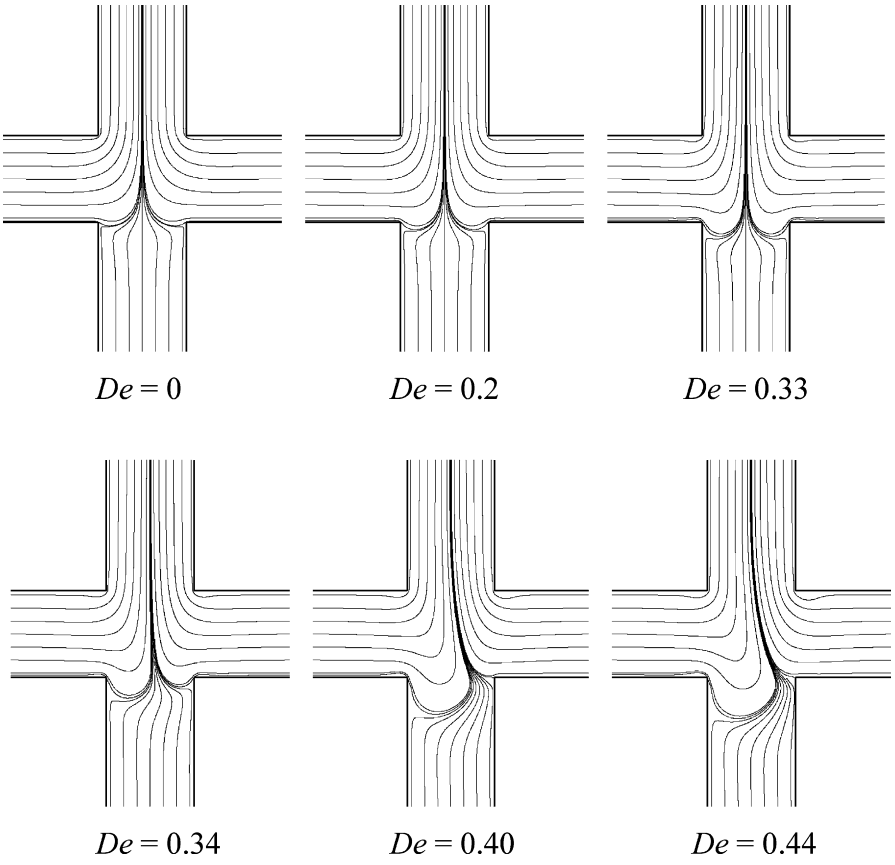

Fig. 2. Effect of Deborah number on the flow patterns ($WR = 1$, $VR = 20$): the onset of a steady-flow asymmetry.

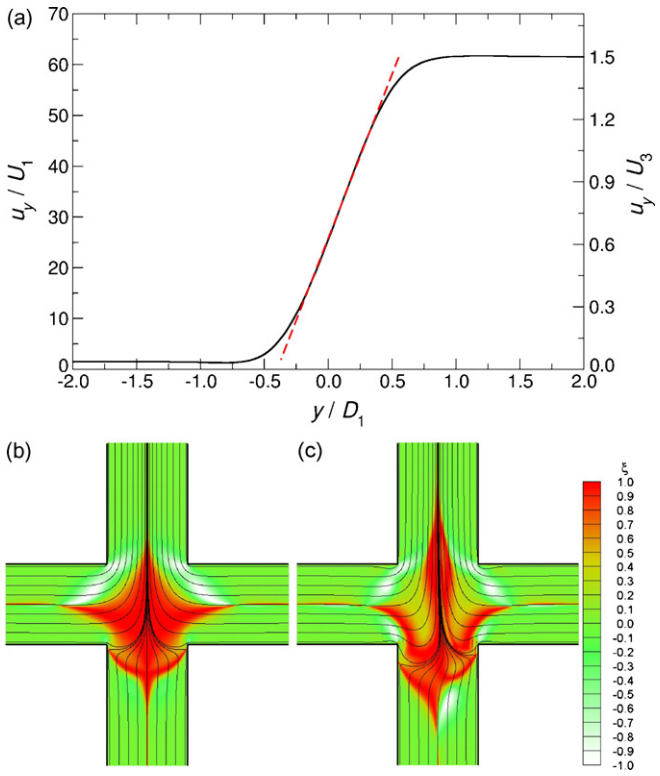

Fig. 3. Extensional flow in the flow-focusing geometry ($WR = 1$, $VR = 20$): axial velocity profile along the centerline ($x = 0$) for $De = 0.1$ (a); contour plot of the flow-type parameter together with corresponding streamline patterns for $De = 0.1$ (b) and for $De = 0.34$ (c).

et al. [17]. In this figure, one can clearly observe the presence of a considerable and well-defined region of extensional flow near the converging section.

Above the critical Deborah number, $De \gtrsim 0.34$, we observe the onset of a steady supercritical pitchfork bifurcation, with the flow becoming increasingly spatially asymmetric as De further increases. Fig. 3c shows a contour plot of the flow-type parameter for conditions under which the flow is asymmetric ($De = 0.34$). Eventually, the flow becomes time-dependent for $De \gtrsim 0.5$. A similar instability was observed experimentally for dilute flexible polymer solutions flowing in a conventional cross-slot geometry [12] and was predicted numerically using a UCM fluid in an analogous geometry [13]. The flow in the cross-slot examined by Poole et al. [13] exhibits a stagnation point at the center of the geometry, where the extensional stresses in the UCM fluid flow become unbounded when the local Weissenberg number exceeds 0.5. A fundamental difference of the current configuration relative to the cross-slot is that in the current flow-focusing device there is no stagnation point and although the axial normal stress (τ_{yy}) grows substantially along the vertical centerline ($x = 0$), as shown in Fig. 4, it is always bounded. This leads us to conclude that the singularity observed in the typical cross-slot cannot be solely responsible for the symmetry-breaking bifurcation. This conclusion is further supported by the recent findings of Rocha et al. [15] using FENE-type models in the cross-slot flow, and by our findings with the PTT model presented below.

The transition to asymmetric flow is only observed for sufficiently high velocity ratios. For $VR \lesssim 5$, the flow evolves from steady and symmetric to unsteady, fluctuating in time without ever exhibiting steady asymmetric behavior. In the limit of high VR ($VR \gtrsim 20$), the critical Deborah number becomes approximately constant, $De_c = 0.335 \pm 0.005$ for $WR = 1$, as shown in Fig. 5. Also

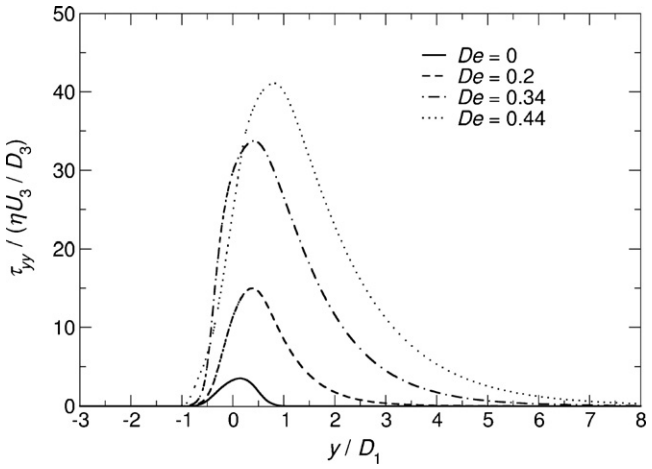

Fig. 4. Axial normal stress profiles along the centerline ($x = 0$) for $WR = 1$, $VR = 20$.

illustrated in Fig. 5 is the critical Deborah number for the onset of unsteady flow, which also becomes approximately constant for high VR, but occurs at a larger value of De ($De_c^* \approx 0.50$).

In order to evaluate the degree of flow asymmetry, we first examine the profile of the y-component of the velocity, u_y, along the lateral direction for $y = -D_2/2$ near the entrance branches. This is shown in Fig. 6a for $WR = 1$, $VR = 20$. For Newtonian fluid flow, the profile is perfectly symmetric with the fluid moving upstream (negative velocities) near the walls and flowing downstream (positive velocities) in the region close to the centerline, where the maximum velocity value is attained. As De increases, the profile retains its symmetry, but the maximum velocity u_y on the centerline increases and the velocity near the wall decreases. Between $0.33 < De_c < 0.34$, steady asymmetric flow sets in and the maximum velocity shifts from the centerline. Increasing De further, the u_y profile becomes increasingly asymmetric with most of the fluid flowing upstream through one half of the channel and flowing downstream through the other half. We should reinforce that here the flow is steady and bistable, i.e. the system has two possible stable solutions, one being the mirror image of the other with respect to $x = 0$. We also note the existence of artificial oscillations of the predicted velocity profiles near $|x/D_1| = 0.5$. These are singular points, and due to the local unbounded nature of pressure and stresses, there is some local detriment of the numerical accuracy. Refining the mesh reduces these local oscillations as shown in Fig. 6b and c. The locally refined mesh near the singular corners demonstrates that, even though the stress and pressure fields are singular, smoother velocity and stress

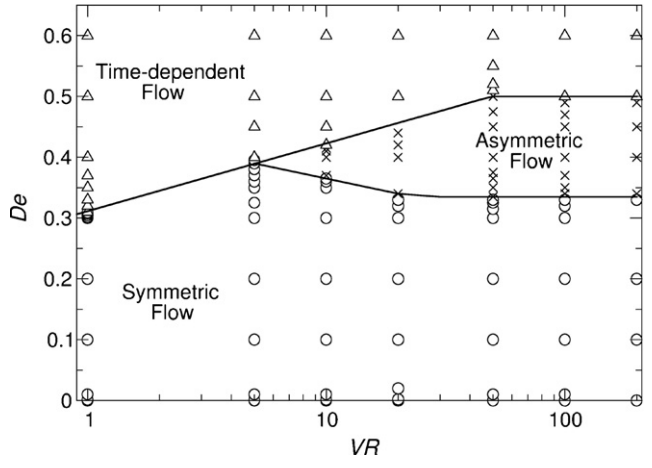

Fig. 5. Flow classification map in the De–VR domain ($WR = 1$).

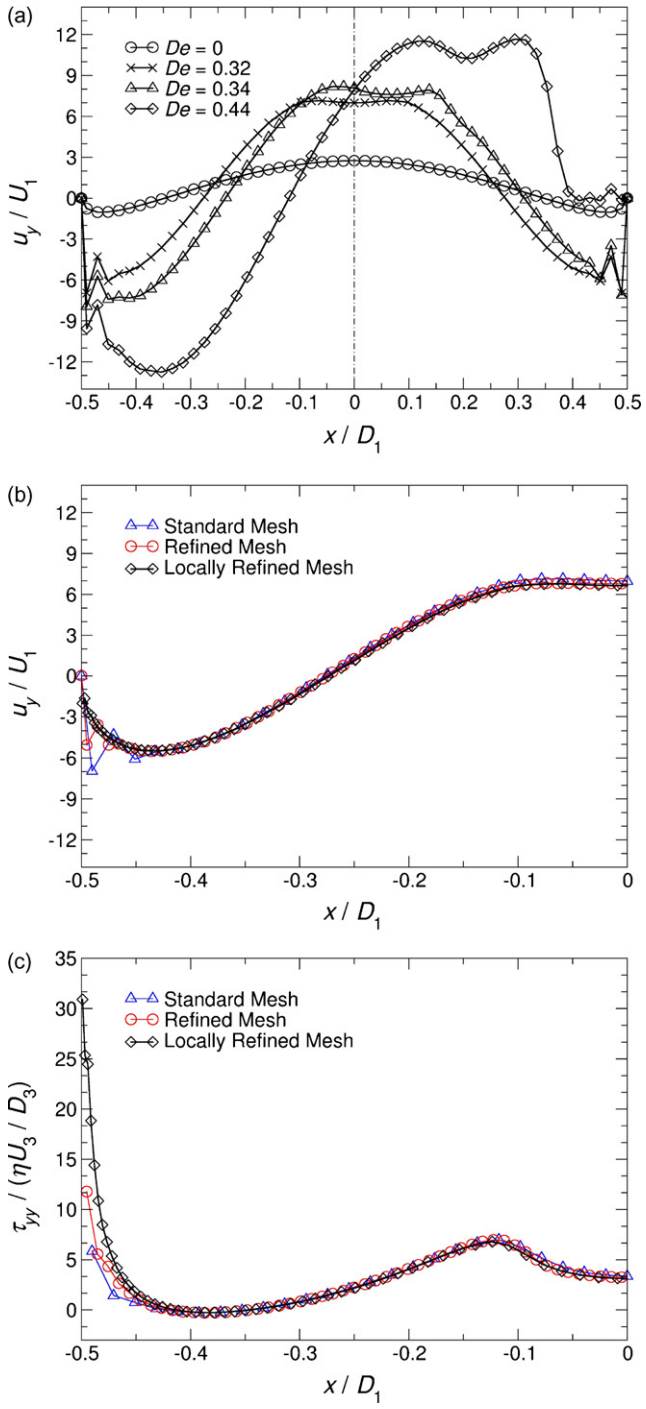

Fig. 6. Profiles along $y = -D_2/2$ ($WR = 1$, $VR = 20$): (a) effect of the Deborah number on the axial velocity profiles; (b) effect of mesh refinement on the axial velocity profile ($De = 0.32$); (c) effect of mesh refinement on the axial normal stress profiles ($De = 0.32$).

profiles are predicted as the mesh is further refined and this is not the cause of the flow asymmetry.

Based on the velocity profiles shown in Fig. 6, we have determined the volumetric fluxes that cross the $y = -D_2/2$ line and calculated an asymmetry parameter, $F^* = (F_W - F_E)/F_3$, to quantify the degree of asymmetry. F_3 is the total flux through the exit branch ($F_3 = Q_3$), F_W is the net flux (taken as positive along the y direction) that passes through half of the mainstream entrance channel 1 between $x = -D_1/2$ and $x = 0$, and F_E is the net flux that passes on the other half of channel 1 between $x = 0$ and $x = +D_1/2$. The net volumet-

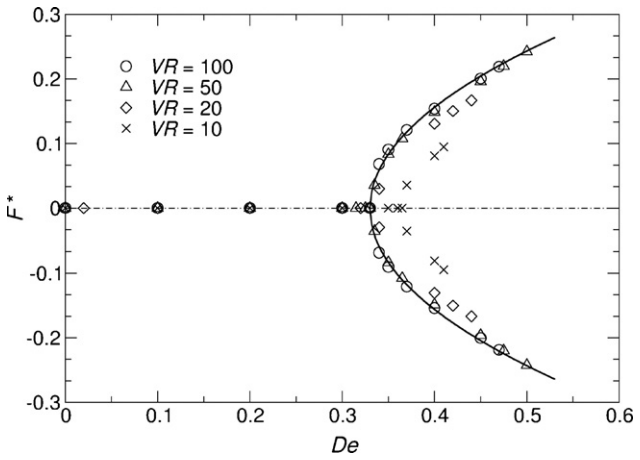

Fig. 7. Bifurcation diagram: effect of the Deborah number on the asymmetry parameter for various VR ($WR = 1$). The solid line represents a square-root fit to the function $F^* = a_1\sqrt{De - De_c}$.

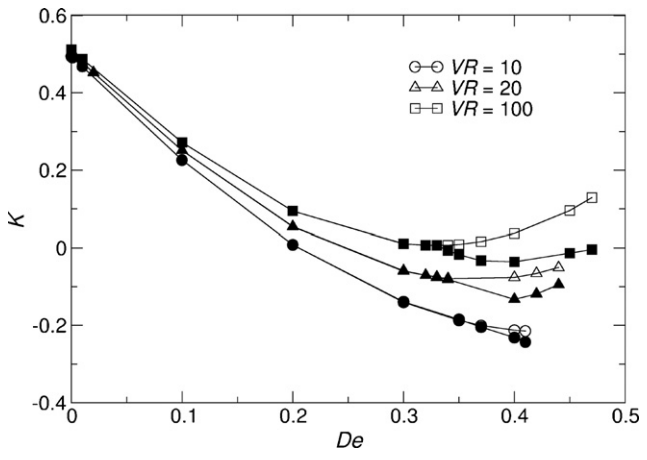

Fig. 8. Comparison of the dimensionless extra-power dissipation for real flow (solid symbols) and symmetry imposed flow (open symbols): $WR = 1$ and various VR.

ric total flux along $y = -D_2/2$ is the same irrespective of whether the flow is symmetric or asymmetric and is equal to the flow rate entering through the central entrance branch: $F_1 = Q_1 = F_E + F_W$. In Fig. 7, we show the bifurcation diagram where we represent the asymmetry parameter F^* as a function of De. The asymmetry parameter is zero when the flow is symmetric and progressively deviates from $F^* = 0$ as the flow becomes increasingly asymmetric. The bistability can be clearly identified in this bifurcation diagram, as can the critical Deborah number (De_c) for the onset of the asymmetry. Interestingly, the data for high VR collapses onto a single curve, which shows not only that De_c becomes constant at high VR (in agreement with the results shown in Fig. 5), but also that the evolution of the asymmetry becomes independent of this parameter. Additionally in Fig. 7, we include a fit to the data for high VR, following a square-root expression, $F* = a_1\sqrt{De - De_c}$, which is typical of pitchfork supercritical bifurcations. For $VR > 20$ and $WR = 1$ we obtain $a_1 = 0.59$ and $De_c = 0.33$.

The existence of a symmetry-breaking bifurcation may be a stress relief mechanism and can be related to minimization of energy dissipation by the flow. Strictly, the principle of free-energy minimization only holds close to thermodynamic equilibrium and therefore the present analysis serves only to show that the energy loss in the device is smaller for a bifurcated flow than for a symmetric flow. To test this hypothesis, we have performed an energy balance in the flow-focusing geometry to evaluate the extra energy dissipation that arises due to the presence of the converging region relative to fully developed flow, and compare it with the corresponding extra-energy dissipation when the flow is forced to be symmetric. In the numerical calculations, we can *artificially* impose symmetry upon the flow to observe the flow behavior in a hypothetical situation in which the onset of asymmetry is precluded. This imposition of symmetry is achieved by performing calculations using only half of the geometry and imposing a symmetry boundary condition along $x = 0$.

The rate of energy dissipation, or power dissipation, $\Delta\dot{W}_{real}$, can be calculated from:

$$\begin{aligned}\Delta\dot{W}_{real} &= Q_1 p_1 + Q_{2W} p_{2W} + Q_{2E} p_{2E} - Q_3 p_3 \\ &= Q_1(p_1 - p_3) + Q_{2W}(p_{2W} - p_3) + Q_{2E}(p_{2E} - p_3)\end{aligned} \tag{6}$$

where the subscripts 1, 2W, 2E and 3 identify the entrance/exit arm (c.f. Fig. 1b) where the variables are evaluated; variable p is the cross-section average pressure in the corresponding channel at a location where the flow is fully developed; and Q is the volumetric flow rate in each arm. $\Delta\dot{W}_{real}$ can be compared to its counterpart under permanent conditions of fully developed viscous flow, given by:

$$\begin{aligned}\Delta\dot{W}_{ideal} &= Q_1 p'_1 + Q_{2W} p'_{2W} + Q_{2E} p'_{2E} - Q_3 p'_3 \\ &= Q_1(p'_1 - p'_0) + Q_{2W}(p'_{2W} - p'_0) + Q_{2E}(p'_{2E} - p'_0) - Q_3(p'_3 - p'_0)\end{aligned} \tag{7}$$

In Eq. (7), the prime designates pressure under fully developed conditions (note that in the present configuration $p_1 = p'_1$, $p_{2W} = p'_{2W}$ and $p_{2E} = p'_{2E}$); p'_0 is the arbitrary pressure at the center of the geometry. This equation may be re-written in terms of the pressure gradient in each arm, assuming that under fully developed flow conditions the pressure loss in the central intersection region is negligible. Thus, we obtain:

$$\begin{aligned}\Delta\dot{W}_{ideal} &= Q_1|dp'/dy|_1 L_1 + Q_{2W}|dp'/dx|_{2W} L_{2W} \\ &\quad + Q_{2E}|dp'/dx|_{2E} L_{2E} + Q_3|dp'/dy|_3 L_3\end{aligned} \tag{8}$$

where L is the distance between the point where the pressure is evaluated and the beginning/end of the corresponding channel, where it opens into the central intersection. The excess power dissipation due to the extensional flow is simply $\Delta\dot{W}_{exc} = \Delta\dot{W}_{real} - \Delta\dot{W}_{ideal}$. In Eqs. (6) and (7) the contributions from the normal stresses were not considered because they will cancel out when calculating the difference between the real and ideal works. In general, the same applies to the kinetic energy, although in our case this contribution is negligible because we are dealing with creeping flows. The excess power dissipation can be rendered dimensionless according to:

$$K = \frac{\Delta\dot{W}_{real} - \Delta\dot{W}_{ideal}}{Q_3\left|dp/dy\right|_3 D_3} \tag{9}$$

Note that by using $\Delta\dot{W}_{real} - \Delta\dot{W}_{ideal}$ instead of $\Delta\dot{W}_{real}$, the results become independent of L as long as L is sufficiently large for fully developed conditions to be attained. Physically, one may think of K as the extra-power dissipation in the flow-focusing device expressed in terms of an equivalent number of downstream channel widths required to generate the same power dissipation in ideal fully developed flow. It is worth noting that for the special case where the flow rate is the same in all inlet channels, Q factors out of Eq. (9), which then becomes equivalent to the so-called Couette correction (commonly used in contraction and expansion flows [28–32]).

The evolution of the dimensionless extra-power dissipation with the Deborah number is shown in Fig. 8 for $WR = 1$ and various VR. For $De = 0$, the value of K calculated numerically is similar

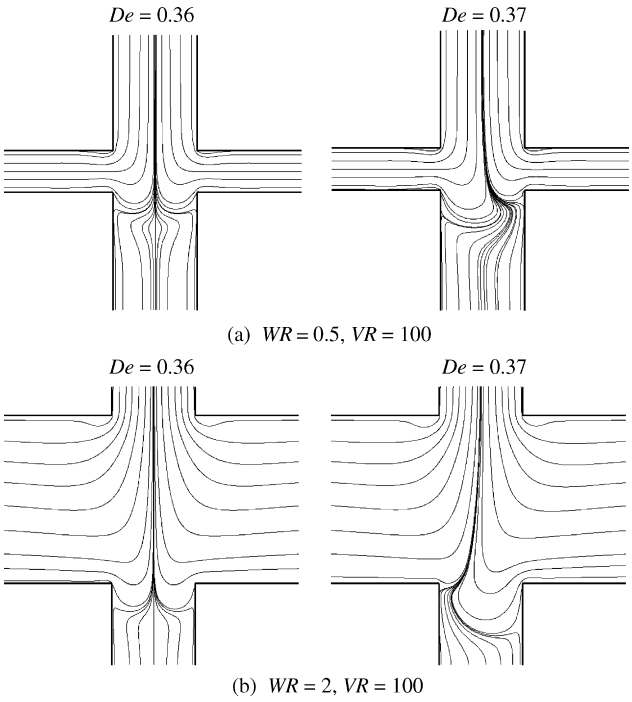

Fig. 9. Flow patterns near the critical Deborah number for different *WR*.

to the value expected for a contraction with an equivalently high contraction ratio [28]. As *De* increases, *K* decreases and in some cases becomes negative, which indicates an energy gain relative to the fully developed flow case ($\Delta\dot{W}_{real} < \Delta\dot{W}_{ideal}$). A similar elastic recovery has been predicted numerically using Oldroyd-B and UCM fluids in contraction flows [20,28]; however no instances of elastic recovery have yet been observed experimentally.

The values of the dimensionless extra-power dissipation for the corresponding forced symmetric flow are shown in Fig. 8 as open symbols. For Deborah numbers below the critical value, the results using the two meshes are obviously identical. Above the critical *De*, the values of *K* obtained by imposing symmetry are higher than those obtained using the full domain. This difference in power dissipation is enhanced for higher *VR* and also for higher *De* as the asymmetry becomes more pronounced. Our results indicate that the viscoelastic flow consumes less energy by bifurcating to asymmetric flow than it would if it were flowing symmetrically. Poole et al. [13] and Rocha et al. [15] reported a similar effect, expressed in terms of a difference in Couette correction, in the flow through a cross-slot configuration. The Couette correction used by Poole et al. [13] is equivalent to the dimensionless excess power dissipation, expressed in Eq. (9), but the present approach is more general, since it allows for cases with multiple streams in which flow rates are different in different sections of the geometry.

In addition to the study of the effect of *VR* on the symmetry-breaking bifurcation, we have also examined the effect of the width ratio. As observed for low *VR* at *WR* = 1, for low *WR* (*WR* ≤ 0.3) steady asymmetric flow is not observed even for very high *VR* and the flow evolves directly from steady symmetric to unsteady as *De* increases. These results suggest that the flow rate ratio, *FR* = *VR*·*WR* (instead of *VR*), might be the controlling variable for the onset of asymmetric flow. The behavior observed for $0.4 \leq WR \leq 2$ is qualitatively similar to that observed for *WR* = 1: at low *De* the flow is symmetric and becomes bistably asymmetric above a critical Deborah number. In Fig. 9, we show flow patterns at sub- and super-critical conditions near De_c for *WR* = 0.5 and *WR* = 2.

The effect of the flow rate ratio on De_c is illustrated in Fig. 10 for various *WR* ($0.4 \leq WR \leq 2$), where the lines are merely used to

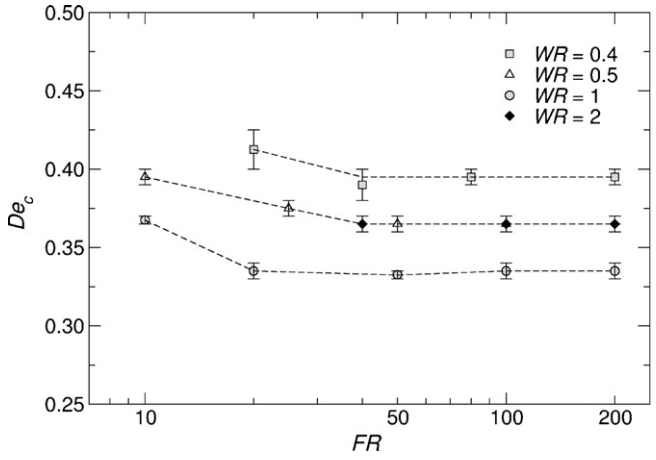

Fig. 10. Effect of the flow rate ratio ($FR \equiv VR \times WR = (U_2D_2)/(U_1D_1)$) on the onset of flow asymmetries for various *WR*. The lines are indicative of the critical Deborah number.

indicate the trends in the critical Deborah number. The error bars represent the highest *De* corresponding to symmetric flow and the lowest *De* at which asymmetric flow was obtained numerically. As for *WR* = 1, De_c also varies with *VR* attaining a constant value for high *VR*. Additionally, it is already apparent that the dependence of De_c on *WR* at high *VR* is non-monotonic. Incidentally, the values of De_c are the same for *WR* and 1/*WR* (e.g. *WR* = 0.5 and *WR* = 2), at least within the range of *WR* studied ($0.4 \leq WR \leq 2$).

The corresponding bifurcation diagrams, obtained in the limit of high *VR*, are shown in Fig. 11. Here one can clearly see that *WR* influences both the value of De_c and the magnitude of the flow asymmetry. Overall, the magnitude of the flow asymmetry increases with decreasing *WR* and the variation of De_c with the width ratio is non-monotonic, as already observed in Fig. 10. To highlight this non-monotonic effect, Fig. 12 shows De_c in the limit of high *VR* as a function of *WR*. The plot exhibits a parabolic shape in semi-log coordinates, with a minimum value of $De_{c,min} \approx 0.335 \pm 0.005$ at *WR* = 1.

As already discussed, we have conducted additional simulations using the PTT model, in order to assess the importance of the extensional properties of the fluid upon the onset of the steady asymmetric flow. We used a solvent ratio of $\beta = 1/9$, a typical value used in numerical studies (e.g. [28]), and varied the extensibility parameter, which is known to have a key influence on the extensional viscosity (at low ε values the steady extensional viscosity is

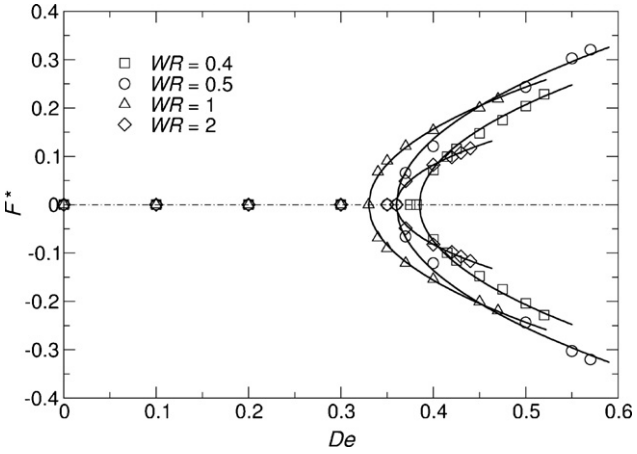

Fig. 11. Effect of *WR* on the bifurcation diagrams obtained in limit of high *VR*. The solid lines represent square-root fits to the function $F^* = a_1\sqrt{De - De_c}$.

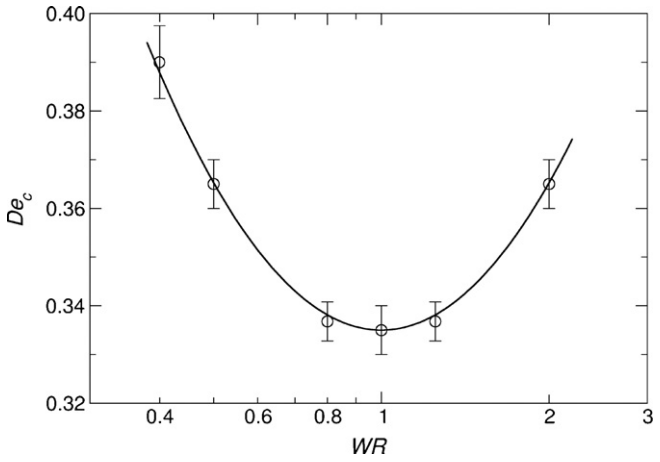

Fig. 12. Critical Deborah number in the limit of high *VR* as a function of *WR*. The line represents a parabolic fit.

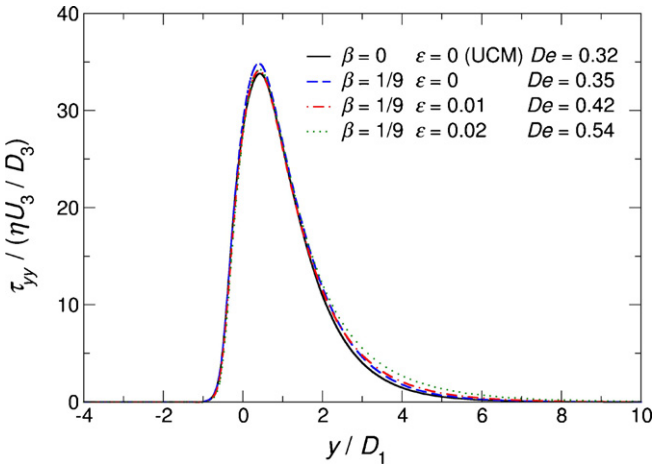

Fig. 14. Axial normal stress profiles along the centerline ($x = 0$) corresponding to the cases shown in Fig. 13 for *De* just below the critical conditions.

inversely proportional to ε). In Fig. 13 we summarize the numerical results in a bifurcation diagram, from which several conclusions can be inferred: (i) for $\varepsilon = 0$, when the Oldroyd-B model is recovered, a small delay in the critical conditions is observed, as compared with the UCM model. A similar behavior was reported for the cross-slot flow instability [33]; (ii) increasing the ε parameter leads to an increase in the critical *De*, and the degree of asymmetry (quantified as F^*) becomes less sensitive to *De*; (iii) for $\varepsilon \geq 0.04$ the steady asymmetry is no longer observed, and the flow transitions directly from steady symmetric to unsteady at much higher *De* values (which further increases as ε increases). These results suggest that the extensional properties of the fluid are decisive for the onset of the flow asymmetry that is observed above a critical *De*, which is related to the development of large normal stresses along the centerline in the converging region. To further establish this hypothesis, in Fig. 14 we plot the axial normal stress profiles along the centerline ($x = 0$) for the cases shown in Fig. 13 that are just below critical conditions. It is clear that similar levels of normal stresses are achieved at critical conditions, highlighting the key role of the extensional properties of the fluid upon the inception of a steady-flow asymmetry.

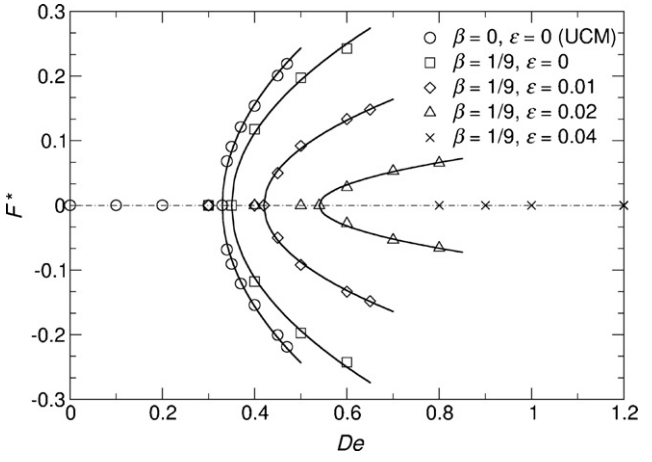

Fig. 13. Effect of the constitutive model and the ε parameter on the bifurcation diagram (*VR* = 100). The solid lines represent square-root fits to the function $F^* = a_1\sqrt{De - De_c}$.

5. Conclusions

We have presented a detailed numerical study of the flow of UCM and PTT fluids through a flow-focusing geometry under creeping-flow conditions, aimed at identifying the onset of flow asymmetries and instabilities as a function of Deborah number, velocity ratio and width ratio. The device is two-dimensional, with a cross-like shape containing three inlets and one outlet. The two opposing lateral inlet streams shape the third main inlet stream producing a converging flow region.

The results obtained with the UCM model show that at low Deborah numbers the flow is symmetric relative to the centerline. Strong viscoelastic effects were observed as the Deborah number increased and the flow was seen to become asymmetric, while remaining steady, for *De* above a critical value. Above an even higher threshold value of the Deborah number, a subsequent instability was identified in which the flow becomes unsteady. For very low *VR* or *WR*, the flow evolves directly from steady symmetric to unsteady, oscillating in time without ever going through the intermediate regime of steady asymmetric flow, since the normal stresses are not sufficiently high to trigger this intermediate transition.

The level of flow asymmetry was quantified using an asymmetry parameter F^* which is a measure of the imbalance of the relative net flux through each side of the main inlet channel close to the central region. As *De* is increased above the critical threshold, the flow becomes increasingly asymmetric and the asymmetry parameter gradually deviates from $F^* = 0$ according to a square-root law, typical of pitchfork supercritical bifurcations $\left(F* = a_1\sqrt{De - De_c}\right)$. The magnitude parameter, a_1, and the critical Deborah number, De_c, depend on both the velocity ratio and the width ratio. However, for sufficiently high velocity ratios, the onset and the evolution of the asymmetry becomes purely geometric, i.e. independent of *VR*. The magnitude of the asymmetry increases with decreasing *WR*, while the variation of De_c with *WR* is non-monotonic.

By performing an energy balance in the flow-focusing geometry we were able to evaluate the dimensionless extra-power dissipation in the device, and compared it with the case in which symmetric flow is artificially imposed. The results suggest that the bifurcation to asymmetric flow is a stress relief mechanism, and demonstrate that the viscoelastic flow consumes less energy by bifurcating to steady asymmetric state than it would if it were flowing symmetrically.

The results obtained using the PTT model reveal that the extensional properties of the fluid are crucial for the onset of the steady asymmetric flow, and the critical *De* increases as ε increases. Above

$\varepsilon = 0.04$ no steady asymmetry is found – the transition to unsteady flow occurs at significantly higher values of *De*, which tend to rise as ε increases further.

Acknowledgements

The authors wish to thank British Council and the Portuguese Council of Rectors for funding through exchange projects B35/08, B10/07 and B11/07. MAA, FTP and MSNO would also like to acknowledge funding provided by Fundação para a Ciência e a Tecnologia and FEDER under projects PPCDT/EME/59338/2004, PTDC/EQU–FTT/71800/2006 and POCI/EME/58657/2004. PJO wishes to thank Universidade da Beira Interior for a sabbatical leave.

References

[1] R.G. Larson, Instabilities in viscoelastic flows, Rheologica Acta 31 (1992) 213.
[2] E.S.G. Shaqfeh, Purely elastic instabilities in viscometric flows, Annual Review of Fluid Mechanics 28 (1996) 129.
[3] R.G. Larson, E.S.G. Shaqfeh, S.J. Muller, A purely elastic instability in Taylor–Couette flow, Journal of Fluid Mechanics 218 (1990) 573.
[4] S.J. Muller, R.G. Larson, E.S.G. Shaqfeh, A purely elastic transition in Taylor–Couette flow, Rheologica Acta 28 (1989) 499.
[5] J.A. Byars, A. Oztekin, R.A. Brown, G.H. McKinley, Spiral instabilities in the flow of highly elastic fluids between rotating parallel disks, Journal of Fluid Mechanics 271 (1994) 173.
[6] J.J. Magda, R.G. Larson, A transition occurring in ideal elastic liquids during shear-flow, Journal of Non-Newtonian Fluid Mechanics 30 (1988) 1.
[7] G.H. McKinley, J.A. Byars, R.A. Brown, R.C. Armstrong, Observations on the elastic instability in cone-and-plate and parallel-plate flows of a polyisobutylene Boger fluid, Journal of Non-Newtonian Fluid Mechanics 40 (1991) 201.
[8] G.H. McKinley, A. Öztekin, J.A. Byars, R.A. Brown, Self-similar spiral instabilities in elastic flows between a cone and a plate, Journal of Fluid Mechanics 285 (1995) 123.
[9] P. Pakdel, G.H. McKinley, Elastic instability and curved streamlines, Physical Review Letters 77 (1996) 2459.
[10] G.H. McKinley, P. Pakdel, A. Öztekin, Rheological and geometric scaling of purely elastic flow instabilities, Journal of Non-Newtonian Fluid Mechanics 67 (1996) 19.
[11] J.A. Pathak, S.D. Hudson, Rheo-optics of equilibrium polymer solutions: worm-like micelles in elongational flow in a microfluidic cross-slot, Macromolecules 39 (2006) 8782.
[12] P.E. Arratia, C.C. Thomas, J. Diorio, J.P. Gollub, Elastic instabilities of polymer solutions in cross-channel flow, Physical Review Letters 96 (2006) 144502.
[13] R.J. Poole, M.A. Alves, P.J. Oliveira, Purely elastic flow asymmetries, Physical Review Letters 99 (2007) 164503.
[14] L. Xi, M.D. Graham, A mechanism for oscillatory instability in viscoelastic cross-slot flow, Journal of Fluid Mechanics 622 (2009) 145.
[15] G.N. Rocha, R.J. Poole, M.A. Alves, P.J. Oliveira, On extensibility effects in the cross-slot flow bifurcation, Journal of Non-Newtonian Fluid Mechanics 156 (2009) 58.
[16] W.-J. Luo, Effect of ionic concentration on electrokinetic instability in a cross-shaped microchannel, Microfluidics and Nanofluidics (2009), 10.1007/s10404-008-0316-2.
[17] M.S.N. Oliveira, F.T. Pinho, M.A. Alves, Extensional flow in a flow-focusing device (in preparation).
[18] N. Phan-Thien, R.I. Tanner, New constitutive equation derived from network theory, Journal of Non-Newtonian Fluid Mechanics 2 (1977) 353.
[19] M.A. Hulsen, R. Fattal, R. Kupferman, Flow of viscoelastic fluids past a cylinder at high Weissenberg number: stabilized simulations using matrix logarithms, Journal of Non-Newtonian Fluid Mechanics 127 (2005) 27.
[20] M.A. Alves, F.T. Pinho, P.J. Oliveira, Effect of a high-resolution differencing scheme on finite-volume predictions of viscoelastic flows, Journal of Non-Newtonian Fluid Mechanics 93 (2000) 287.
[21] P.J. Oliveira, F.T. Pinho, G.A. Pinto, Numerical simulation of non-linear elastic flows with a general collocated finite-volume method, Journal of Non-Newtonian Fluid Mechanics 79 (1998) 1.
[22] R. Fattal, R. Kupferman, Constitutive laws for the matrix-logarithm of the conformation tensor, Journal of Non-Newtonian Fluid Mechanics 123 (2004) 281.
[23] A.M. Afonso, P.J. Oliveira, F.T. Pinho, M.A. Alves, The log conformation tensor approach in the finite volume method framework, Journal of Non-Newtonian Fluid Mechanics 157 (2009) 55.
[24] D.O.A. Cruz, F.T. Pinho, P.J. Oliveira, Analytical solutions for fully-developed laminar flow of some viscoelastic liquids with a Newtonian solvent contribution, Journal of Non-Newtonian Fluid Mechanics 132 (2005) 28.
[25] G. Astarita, Objective and generally applicable criteria for flow classification, Journal of Non-Newtonian Fluid Mechanics 6 (1979) 69.
[26] G. Mompean, R.L. Thompson, P.R.S. Mendes, A general transformation procedure for differential viscoelastic models, Journal of Non-Newtonian Fluid Mechanics 111 (2003) 151.
[27] R.L. Thompson, P.R.S. Mendes, M.F. Naccache, A new constitutive equation and its performance in contraction flows, Journal of Non-Newtonian Fluid Mechanics 86 (1999) 375.
[28] M.A. Alves, P.J. Oliveira, F.T. Pinho, Benchmark solutions for the flow of Oldroyd-B and PTT fluids in planar contractions, Journal of Non-Newtonian Fluid Mechanics 110 (2003) 45.
[29] D.V. Boger (Ed.), Circular Entry Flows of Inelastic and Viscoelastic Fluids, Wiley Eastern, New Delhi, 1982.
[30] M.S.N. Oliveira, L.E. Rodd, G.H. McKinley, M.A. Alves, Simulations of extensional flow in microrheometric devices, Microfluidic and Nanofluidic 5 (2008) 809.
[31] P.J. Coates, R.C. Armstrong, R.A. Brown, Calculation of steady-state viscoelastic flow through axisymmetrical contractions with the EEME formulation, Journal of Non-Newtonian Fluid Mechanics 42 (1992) 141.
[32] R.J. Poole, M.A. Alves, P.J. Oliveira, F.T. Pinho, Plane sudden expansion flows of viscoelastic liquids, Journal of Non-Newtonian Fluid Mechanics 146 (2007) 79.
[33] R.J. Poole, M.A. Alves, A. Afonso, F.T. Pinho, P.J. Oliveira, Purely elastic instabilities in a cross-slot flow, in: The Society of Rheology 79th Annual Meeting, Salt Lake City, USA, October 7–11, 2007.